Fission channels for fragment isotopes from ^{298}Fl with magic nucleon numbers

R. A. Gherghescu ●* and D. N. Poenaru ●

Department for Theoretical Physics, Horia Hulubei National Institute for Physics and Nuclear Engineering, Bucharest-Magurele RO-077125, Romania

Short-lived systems such as superheavy nuclei decay mainly by α emission. However, fission fragment emission is also probable, as theoretical calculations prove it. ^{298}Fl dynamics decay is studied with a specialized binary macroscopic-microscopic method combined with the mass inertia tensor. The multidimensional WKB tunneling method is used to obtain the penetrabilities and half-lives. The calculations are applied to fission channels around the isotopes of two presumably favored fragments, Pb and Sn. The choice is due to their proton magicity shell correction favorable fission valleys.

I. INTRODUCTION

The dynamics of the spontaneous fission process is accepted as being a mostly adiabatic motion. In this respect, one mainly considers two major steps when approaching the phenomena: the statical part, which involves the calculation of the deformation energy and the dynamical one, which presumes the mass inertia tensor and half-life calculations, supposing a tunneling action takes place. A considerable amount of work has been devoted to the subject. Some of them will be recalled here. Recently, the efforts have been directed towards possible fission of superheavy elements, as a complement to α decay. The most utilized method is still the macroscopic-microscopic one. Under this picture, the fission takes place as the Coulomb repulsion overcomes the nuclear surface tension forces. In addition, the shell effects generated by the transition of the levels schemes from one parent towards separated wells come into play. This algorithm of calculation has been used by many groups at the time, mostly considering only one-center shell potential submitted to various deformations until the exit point is reached. In Ref. [1], the macroscopic-microscopic method is used, with the Yukawa-plus-exponential model for the macroscopic part and, alternatively, a simplified two-center oscillator or a generalized Woods-Saxon as the single-particle potentials. The dynamics is completed by the irrotational flow inertia tensor or cranking approximation. Spontaneous fission half-lives are calculated by considering the fission barrier penetration in a multidimensional deformation space $\{\beta_\lambda\}$ for axial symmetry [2]. The potential energy is calculated by the macroscopic-microscopic method. The cranking inertia is used as the mass tensor. The barrier is formed here by the variation of the β parameters within a single nucleus potential. Heavy and superheavy nuclei ($Z = 92$–110) are studied. The usual WKB

approximation is used to obtain the penetrabilities. The fission trajectory is obtained this way, with no fission channel mentioned, but within a very large space of deformation. The analysis becomes more complex as the space of deformation is larger. To this end, the fission dynamics is treated in a multidimensional space with axial deformation [3]. The deformation energy is obtained from the macroscopic-microscopic approach, with the Yukawa-plus-exponential model for the macroscopic part and the Strutinsky shell corrections based on the Woods-Saxon single-particle potential for the microscopic part. All possible paths are calculated within a multidimensional grid and the one corresponding to the lowest value is chosen as the fission path. The same method, using the same potentials, has been used to provide the fission barrier for superheavy nuclei [4]. Conclusions are drawn here from the height of the barrier for different superheavy fissioning nuclei. Another successful method proved to be the stochastic Langevin approach. The set of Langevin equations provide the possibility to calculate the fission probability and multiplicities of evaporating prescission particles, as well as the fragment mass distribution. The dynamics of the fission process is treated in a review [5] also within this method and the formation of fission fragment mass, energy, charge, and angular distributions is stressed within solving the Langevin equations. It also provides the dynamics of uranium and plutonium, together with the macroscopic-microscopic energy and irrotational mass tensor [6]. This work is somehow related to the actual results presented here, since it gives the possibility to discern from different charge asymmetries, besides the mass ones. A more complex macroscopic-microscopic method has been employed recently, providing the potential energy surfaces for even-even superheavy nuclei [7]. An effective liquid drop mass formula determines the macroscopic part and the Strutinsky shell corrections completes the statical term. The dynamics follows with the WKB penetrability calculation. The mass parameter is taken as a phenomenological collective inertia and the usual formula for spontaneous fission half-life is used. The already well-known quantum

---

*Frankfurt Institute for Advanced Studies, J. W. Goethe University, Frankfurt am Main, Germany; radu@theory.nipne.ro

mechanical fragmentation theory (QMFT) from Ref. [8] is applied to study the fission of the lighter ^{76}Sr, in Ref. [9]. The model uses the usual macroscopic terms, the nuclear and Coulomb ones. The shell effects are accounted for as in Ref. [10]. Following the experimental binding energies entering in the potential, the model accounts for certain fragmentation channels. It is also a reason why this work is related to the present calculations. The reduced mass is used to complete the fission dynamics. The same QMFT approach is used in Ref. [11], where the total deformation energy consists in the sum of the ground-state binding energies, the Coulomb and the nuclear proximity potential. The tunneling probability is split here in the internal region, up to the Süssmann radius, the second one up to the second turning point. As for the mass inertia, the reduced mass is used again as a simplification in the WKB procedure. A largely used method is the generalized liquid drop model for the calculation of the fission barriers [12]. Penetrabilities are obtained using the reduced mass as the inertia tensor. The same approach using more elaborate shapes such as elliptic lemniscatoids is presented in Ref. [13]. A somehow modified generalized liquid drop model is employed to study the decay of superheavy nuclei in the range $104 \leqslant Z \leqslant 118$ in Ref. [14]. Shell effects are considered from Ref. [15]. The dynamics is finalized with the mass inertia calculated for the rigid body approximation [16]. Again, the WKB tunneling formula provides the penetrability and further more, the fission half-life. Coulomb and proximity potentials are used again in the macroscopic-microscopic algorithm for deformed nuclei [17]. A new shell-effect-dependent formula is used for the fission half-lives. The dynamics is simplified by taking the reduced mass as the inertia tensor. This kind of approach gives a good estimation for the α-decay lifetimes from superheavy elements [18]. A reasonable reduced mass replaces here again the mass tensor, taking into account the α dimensions against the superheavy one. The decay half-lives are also calculated in the formalism of a nucleus-nucleus potential obtained by folding the densities of interacting fragments within the DDM3Y effective nuclear interaction [19]. In the tunneling probability framework, the reduced mass is once more used as a simplified alternative to the inertia tensor. Even though the shell corrections are phenomenologically taken into account, the results describe the experimental data in a satisfactory way. Dissipation is added to the dynamical evolution of nuclear fission in Ref. [20]. The tensors are calculated for a large variety of nuclear shapes with the Werner-Wheeler approximation for incompressible flow. As it is generally the case, calculations are made for axially symmetric shapes, in cylindrical coordinates. Real-time fission dynamics from low-energy to high excitations in ^{240}Pu is studied within the time-dependent Hartree-Fock + BCS method [21]. The fission yields can be divided here into two asymmetric scission channels: an average mass of $A_H \approx 135$ and 138.7, as being the distribution of mass asymmetry, a little far from $A_H = 132$ as double magic. Finally, a different approach for the decay problem is presented by a universal decay law [22]. The electrostatic interaction, asymmetry, and angular momentum are utilized in the dynamics to estimate the half-lives of α decay.

These works have been mentioned especially due to their link to the dynamics of the fission process. Different approaches are able to give information about the stability of nuclei against fission, barriers, and half-lives. The present work explores the probability of a certain fission channel, characterized by both charge and mass asymmetry at the same time. Calculations are applied to possible favored fission reactions from ^{298}Fl. Sections II and III present the theoretical background of the calculations, whereas Sec. IV is devoted to the results and discussions, followed by conclusions.

II. BINARY MACROSCOPIC-MICROSCOPIC METHOD

A highly specialized macroscopic-microscopic method has been established to account for the binary character of the fission process. The model provides the possibility to follow a certain fission channel, mass, and charge given asymmetry at the same time, from the initial parent nucleus, going through the overlapping part, up to two totally separated nuclei. The statical part, namely the fission barrier, is built from the two well-known parts: the charged liquid drop deformation energy, as the macroscopic one, and the shell corrections as the microscopic effect of the discrete level schemes. The first term must bear the binary character of the process, so interacting energy terms will be added to the macroscopic part, as being geometry and charge density dependent. The last one is generated by the configuration of the interacting proton and neutron level schemes, from the compound nucleus single potential, through two partially interacting up to finally separated deformed potential wells. The proton and neutron level schemes thus calculated will be input data for the shell correction computation.

The dynamical part comprises first the introduction of the inertia tensor as a totally deformation-dependent quantity. Then the final step consists in the calculation of the fission penetrability of a given exit channel followed by the half-lives. Each of these steps is presented in the following sections.

A. Binary deformed charged liquid drop energy

The macroscopic term is built as the energy of a charged liquid drop with finite range nuclear forces on the nuclear surface. The Yukawa-plus-exponential model will be particularized to binary configuration. Such features will describe each region of the intersected fragment configuration separately, plus the term responsible for the interaction between them. The only deformation-dependent macroscopic terms are the Coulomb E_C and the nuclear surface tension energy E_{YE}, of the Yukawa-plus-exponential type. Thus, the deformation macroscopic energy reads:

$$E_{\text{mac}} = \left(E_C - E_C^{(0)}\right) + \left(E_{YE} - E_{YE}^{(0)}\right). \quad (1)$$

The macroscopic barrier will rise when the nuclear surface term exceeds the electrostatic one. The two terms will be adapted to the binary configuration. The electrostatic Coulomb energy is calculated as:

$$E_C = \frac{2\pi}{3}\left(\rho_{eH}^2 F_{CH} + \rho_{eL}^2 F_{CL} + 2\rho_{eH}\rho_{eL}F_{CHL}\right). \quad (2)$$

The first two terms account for the heavy and light fragment regions, as the last one is introduced as the electrostatic

interaction between the first two. ρ_{eH} and ρ_{eL} are the charge densities. In order to follow the pass from the parent to the final fragments values, a law of variation is introduced as:

$$\rho_{eH} = \frac{Z_{1X}(V_H)}{\frac{4\pi}{3}a_H b_H^2} \quad \rho_{eL} = \frac{Z_{2X}(V_L)}{\frac{4\pi}{3}a_L b_L^2} \tag{3}$$

in electric charge units, and where V_H and V_L are the intermediary heavy and light volumes of the fission configuration, and:

$$Z_{Hx}(V_H) = \frac{V_H}{V_0 - V_{H0}}\left[(V_H - V_{H0})\frac{Z_0}{V_0} + (V_0 - V_H)\frac{Z_{H0}}{V_{H0}}\right] \tag{4}$$

and for the light fragment:

$$Z_{Lx}(V_L) = \frac{V_L}{V_0 - V_{L0}}\left[(V_L - V_{L0})\frac{Z_0}{V_0} + (V_0 - V_L)\frac{Z_{L0}}{V_{L0}}\right]. \tag{5}$$

Here V_0, V_{H0}, and V_{L0} are the separated volumes of the parent, heavy, and light fragment nuclei. V_H and V_L are the volumes of the partially overlapped fragments. At the beginning, the charge densities equal the compound nucleus value. As the splitting advances (the distance between centers R increases), both heavy and light fragment approach their final values, corresponding to the separated configuration. Consequently, the charge densities follow the same trend, according to the above law of variation: when $V_H = V_{H0}$, the intermediary atomic number $Z_{Hx} = Z_H$, as the final value, whereas at the start of the fission process one has: $V_H = V_0$. The same is valid for the light fragment. Of course, the two equations are related through the nuclear volume conservation. In this way, the charge densities will change according to the shape configuration from the parent nucleus ($\approx Z_0/A_0$) up to the final ρ_{eH0} and ρ_{eL0}, for separated fragments. In this way, one imposes the binary character of the process upon the Coulomb term. F_{CH}, F_{CL}, and F_{CHL} are integrals, which depend only on the geometry of the shape:

$$F_{CH} = \int_{-a_1}^{z_s} dz \int_{-a_1}^{z_s} dz' G_H(z, z')$$

$$F_{CL} = \int_{z_s}^{R+a_2} dz \int_{z_s}^{R+a_2} dz' G_L(z, z')$$

$$F_{CHL} = \int_{-a_1}^{z_s} dz \int_{z_s}^{R+a_2} dz' G_{HL}(z, z'). \tag{6}$$

The limits are a_1, a_2, the spheroids semiaxes along the symmetry axis, z_s is the separation point, and R is the distance between centers. The integrands are rather complicated expressions, depending on first and second degree elliptic integrals [23]. For the initial spherical shape, the Coulomb term is

$$E_{C_0} = \frac{3Z^2 e^2}{5r_0 A^{1/3}}. \tag{7}$$

The finite-range nuclear forces produce the Yukawa-plus-exponential energy E_{YE}. Again, one will introduce the binary characteristic term of the interaction [24]:

$$E_{YE} = \frac{1}{4\pi r_0^2}[c_{sH}D_{Y_H} + c_{sL}D_{Y_L} + 2(c_{sH}c_{sL})^{1/2}D_{Y_{HL}}]. \tag{8}$$

The last term is responsible for the nuclear tension interaction between the emerging fragments. The involved expressions are [25]

$$D_{Y_H} = \int_0^{2\pi} \int_{-a_1}^{z_s} \int_{-a_1}^{z_s} E_{Y_H}^{(1)} E_{Y_L}^{(1)} Q^{(1)} d\phi dz dz' \tag{9}$$

$$D_{Y_L} = \int_0^{2\pi} \int_{z_s}^{R+a_2} \int_{z_s}^{R+a_2} E_{Y_H}^{(2)} E_{Y_L}^{(2)} Q^{(2)} d\phi dz dz' \tag{10}$$

$$D_{Y_{HL}} = \int_0^{2\pi} \int_{-a_1}^{z_s} \int_{z_s}^{R+a_2} E_{Y_H}^{(12)} E_{Y_L}^{(12)} Q^{(12)} d\phi dz dz'. \tag{11}$$

The Y + E integrands are only shape dependent:

$$E_{Y_H}^{(i)} = \rho_i^2(z) - \rho_i(z)\rho_i(z')\cos\phi - 0.5(z - z')\frac{d\rho_i^2(z)}{dz}$$

$$E_{Y_L}^{(i)} = \rho_i^2(z') - \rho_i(z)\rho_i(z')\cos\phi + 0.5(z - z')\frac{d\rho_i^2(z')}{dz'}$$

$$Q^{(i)} = 2 - \left[\left(\frac{\sigma_i}{a}\right)^2 + 2\frac{\sigma_i}{a} - 2\right]e^{-\frac{\sigma_i}{a}} \cdot \frac{1}{\sigma_i^4} \tag{12}$$

with $i = H, L$, and $a \approx 0.68$ fm is the range of the nuclear force. A similar expression is valid for the light fragment. $\rho_i(z)$ is the nuclear surface equation in cylindrical coordinates. The σ function depend on geometry:

$$\sigma_i = \left[\rho_i^2(z) + \rho_i^2(z') - 2\rho_i(z)\rho_i(z')\cos\phi + (z - z')^2\right]^{1/2}. \tag{13}$$

The term ensuring the Y + E interaction between the heavy (H) and light (L) fragments in the overlapping region reads:

$$E_{Y_H}^{(HL)} = \rho_H^2(z) - \rho_H(z)\rho_L(z')\cos\phi - 0.5(z - z')\frac{d\rho_H^2(z)}{dz}$$

$$E_{Y_L}^{(HL)} = \rho_L^2(z') - \rho_H(z)\rho_L(z')\cos\phi + 0.5(z - z')\frac{d\rho_L^2(z')}{dz'}$$

$$Q^{(HL)} = 2 - \left[\left(\frac{\sigma_{HL}}{a}\right)^2 + 2\frac{\sigma_{HL}}{a} - 2\right]e^{-\frac{\sigma_{HL}}{a}} \cdot \frac{1}{\sigma_{HL}^4}. \tag{14}$$

For the spherical Y + E term E_{YE}^0:

$$E_Y^{(0)} = \left\{1 - 3\left(\frac{a}{R_0}\right)^2 + \left(\frac{R_0}{a} + 1\right)\left[2 + 3\frac{a}{R_0}\right.\right.$$
$$\left.\left. + 3\left(\frac{a}{R_0}\right)^2\right]e^{-\frac{2R_0}{a}}\right\}E_S^{(0)}. \tag{15}$$

In this way, the macroscopic part is particularized for binary shapes, typically of fission configurations.

B. Deformed two-center shell model

The fission configuration is microscopically defined by two deformed proton and two neutron level schemes, partially overlapped. The two potential wells in interaction generate the necessary energy levels for the computation of the shell corrections. Such demands are fulfilled by the deformed two-center shell model (DTCSM) [26]. The main ingredients of the model are based on two intersected Nilsson-type potentials. The core of the two-well potential model, $V_{DTCSM}(\rho, z)$

consists in two deformed interacting oscillators, defined by two partially overlapped spheroids. The residual interactions of spin-orbit $V_{\hat{l}\hat{s}}$ and squared angular momentum $V_{\hat{l}^2}$ potentials are added for the more realistic behavior. The total

Hamiltonian of the model reads:

$$H_{DTCSM} = \frac{\hbar^2}{2m_0}\Delta + V_{DTCSM}(\rho, z) + V_{\hat{l}\hat{s}}(\rho, z) + V_{\hat{l}^2}(\rho, z),$$
(16)

where:

$$V_{DTCSM}(\rho, z) = \begin{cases} V_H(\rho, z) = \frac{1}{2}m_0\omega_{\rho H}^2\rho^2 + \frac{1}{2}m_0\omega_{z_H}^2(z + z_H)^2, & \text{for } A_H - \text{region} \\ V_L(\rho, z) = \frac{1}{2}m_0\omega_{\rho L}^2\rho^2 + \frac{1}{2}m_0\omega_{z_L}^2(z - z_L)^2, & \text{for } A_L - \text{region} \end{cases}$$
(17)

$$V_{\hat{l}\hat{s}} = \begin{cases} -\left\{\frac{\hbar}{m_0\omega_{0H}}\kappa_H(\rho, z), (\nabla V_{DTCSM} \times \hat{p})\hat{s}\right\}, & A_H - \text{region} \\ -\left\{\frac{\hbar}{m_0\omega_{0L}}\kappa_L(\rho, z), (\nabla V_{DTCSM} \times \hat{p})\hat{s}\right\}, & A_L - \text{region} \end{cases}$$

and:

$$V_{\hat{l}^2} = \begin{cases} -\left\{\frac{\hbar}{m_0^2\omega_{0H}^3}\kappa_H\mu_H(\rho, z), (\nabla V_{DTCSM} \times \hat{p})^2\right\}, & A_H - \text{region} \\ -\left\{\frac{\hbar}{m_0^2\omega_{0L}^3}\kappa_L\mu_L(\rho, z), (\nabla V_{DTCSM} \times \hat{p})^2\right\}, & A_L - \text{region} \end{cases} .$$

The binary character of the process is included in the involved quantities: the four frequencies in V_{DTCSM} depend on the spheroidal deformation, by assuming the same value of potential on the nuclear surface: $0.5m_0\omega_{\rho_i}^2a_i^2\eta_i^2 = 0.5m_0\omega_{z_i}^2a_i^2a_i^2 = V_0$ (sphere), which is roughly ≈ 27.25 MeV. η is the semiaxis ratio of each spheroidal fragment.

The anticommutator is used for the residual interactions since the strengths of the spin-orbit $\kappa(z)$ and $\hat{l}^2$ potential, $\mu(z)$ are region dependent. To this end, a geometrical law has been imposed for the pass from the parent nucleus to the final heavy and light fragment strength values, and anticommutator is necessary to make the $V_{\hat{l}\hat{s}}$ and $V_{\hat{l}^2}$ operators self-adjoint.

The basis is obtained for the two-center oscillators:

$$\Phi_m(\phi) = \frac{1}{\sqrt{2\pi}}\exp(im\phi)$$

$$R_{n_\rho}^{|m|}(\rho) = \sqrt{\frac{2\Gamma(n_\rho + 1)\alpha_1^2}{\Gamma(n_\rho + |m| + 1)}}\exp\left(-\frac{\alpha_1^2\rho^2}{2}\right)(\alpha_1^2\rho^2)^{\frac{|m|}{2}}L_{n_\rho}^{|m|}(\alpha_1^2\rho^2)$$

$$Z_\nu(z) = \begin{cases} C_{\nu_1}\exp\left[-\frac{\alpha_1^2(z+z_1)^2}{2}\right]H_{\nu_1}[-\alpha_1(z + z_1)], & z < 0 \\ C_{\nu_2}\exp\left[-\frac{\alpha_2^2(z-z_2)^2}{2}\right]H_{\nu_2}[\alpha_2(z - z_2)], & z \geqslant 0 \end{cases} .$$
(18)

Finally the energy levels are calculated by diagonalization of the residual potential matrix. The proton and neutron level schemes, obtained in this way will carry the influence of the shape configuration on every step along the elongation process.

C. Shell corrections

The shell corrections make the existence of superheavy nuclei possible. The macroscopic barrier is almost nonexistent due to the strong Coulomb repulsion. Negative shell corrections generate a first minimum in the total energy value, which accommodates the ground state of the superheavy system. Once the energy levels are obtained, the shell corrections E_{sh} are separately calculated for protons E_{shp} and neutrons E_{shn}. The Strutinsky main idea is to subtract from the sum of the level energies, protons, and neutrons, an averaged term obtained when a smoothed level distribution is supposed:

$$E_{sh_{p,n}} = \sum_{\nu=1}^{n} 2E_{\nu_{p,n}} - \tilde{U}_{p,n}.$$
(19)

The two corrections are added to get the total energy E_{sh}:

$$E_{sh} = E_{shp} + E_{shn}.$$
(20)

The main quantity here is $\tilde{U}$, the smoothed distribution energy. One needs first the smoothed-level density $\tilde{g}(\epsilon)$ at every step of the splitting, obtained by an averaging procedure:

$$\tilde{g}(\epsilon) = \int_{-\infty}^{\infty}\zeta\left(\frac{\epsilon - \epsilon'}{\gamma}\right)g(\epsilon') = \frac{1}{\gamma}\sum_i\zeta\left(\frac{\epsilon - \epsilon_i}{\gamma}\right)$$
(21)

over an energy range $\gamma \approx \hbar\omega_0$, and $\{\epsilon_i\}$ are the discrete energy levels. The smoothing function:

$$\zeta(x) = \frac{1}{\sqrt{\pi}}e^{-x^2}\sum_{k=0}^{m}a_{2k}H_{2k(x)}$$
(22)

smears every level under a Gaussian, so that finally one gets an almost continuous distribution over the energy levels. Here $H_j(x)$ are the Hermite functions. The smoothed energy goes up to the smoothed Fermi level $\tilde{\lambda}$, a limit obtained from the

nucleon number conservation:

$$N_p = 2 \int_{\infty}^{\tilde{\lambda}} \tilde{g}(\epsilon) d\epsilon. \tag{23}$$

The final term $\tilde{U}$ is calculated:

$$\tilde{U}_{p,n} = 2 \int_{-\infty}^{\tilde{\lambda}_{p,n}} \tilde{g}_{p,n}(\epsilon)\epsilon \, d\epsilon. \tag{24}$$

One has to underline the binary influence on the shell corrections: the proton and neutron levels bear the fragment intrinsical deformation and the degree of splitting within the discrete energy schemes. The involved quantities are functions of the fission shape configuration through the $(a_H, b_H; a_L, b_L; R)$ set, at every step along the distance between centers R.

The final fission barrier E_b is calculated as the total sum of the charged liquid drop and shell correction energies, along the whole range of elongation from parent up to two separated fragments:

$$E_b = E_{mac} + E_{sh}. \tag{25}$$

III. DYNAMICS

The fission such as nuclear shape distortion is governed by the least-action trajectory in the space of deformation coordinates. This reasoning leads to the Wentzel-Kramers-Brillouin procedure, where the mass tensor connection to the general form of the kinetic energy, thence to the action integral, is compulsory. In this work the mass tensor is calculated with a binary Werner-Wheeler algorithm, appropriated to the two-center model fission trajectory. The cranking approximation can also be used, but it has been shown that the cranking and the hydrodynamical masses give similar results for heavier nuclei [27]. Within the irrotational flow of an incompressible, nonviscous fluid, the kinetic energy reads:

$$T = \frac{1}{2} \sum_{i,j} B_{ij} \dot{\alpha}_i \dot{\alpha}_j \tag{26}$$

with the tensor defined as:

$$B_{ij} = \pi \sigma_m \int_{z_m}^{z_M} T_{ij}(z; q_1, \ldots, q_N) dz, \tag{27}$$

where one follows the Wheeler assumption:

$$T_{ij}(z; q) = \rho_s^2(z; q) \left[X_i(z) X_j(z) + \frac{1}{8} \rho_s^2(z; q) \frac{\partial X_i}{\partial z} \frac{\partial X_j}{\partial z} \right]. \tag{28}$$

σ_m is the mass density and q is the set of free deformation coordinates $(a_H, b_H; a_L, b_L; R)$. One has to stress that the semiaxes of the two spheroids are free parameters along the fission trajectory, except for the initial and separated fragment configurations. For binary configurations one

reads [28]:

$$X_i^{(H)}(z) = \frac{1}{\rho_s^2(z; q)} \frac{\partial}{\partial q_i} \int_z^{z_M} \rho_s^2(z'; q) dz'$$

$$X_i^{(L)}(z) = -\frac{1}{\rho_s^2(z; q)} \frac{\partial}{\partial q_i} \int_{z_m}^z \rho_s^2(z'; q) dz' \tag{29}$$

and the final value comes out adding the two:

$$X_i = X_i^{(H)} + H_i^{(L)}, \tag{30}$$

where $\rho_s(z, q)$ is the binary surface shape equation in cylindrical coordinates, due to axial symmetry. The binary mass tensor term calculated from the center of the heavy fragment is B'_{ij}:

$$B'_{ij} = \int_{z_m}^{z_M} T_{ij}(z; q) dz = \int_{-a_1}^{z_c} T_{ij}^{(-)}(z') dz'$$

$$+ \int_{z_c}^{R+a_2} T_{ij}^{(+)}(z') dz'. \tag{31}$$

Since the Wheeler assumption is valid in the center of mass, but the shape is described from the center of the heavy fragment ($z = -z_H$), a correction term B_{ij}^c must be added to the B_{ij} values:

$$B_{ij}^c = \frac{\sigma_m^2 \pi^2}{M} \left\{ \left[\int_{z_m}^{z_M} \rho_s^2(z) X_i(z) dz \right] \left[\int_{z_m}^{z_M} \rho_s^2(z') X_j(z') dz' \right] \right\}. \tag{32}$$

B_{ij}^c corrects the total value for the displacement of the mass center in B'_{ij}. Finally, the components of the inertia mass tensor are calculated as:

$$B_{ij} = B'_{ij} - B_{ij}^c. \tag{33}$$

In order to calculate the final action integral, the tensor components are contracted along the center of mass distance between centers R. This is done by imposing an R-dependent law of variation for the three free coordinates:

$$b_L = b_L(b_0, b_{L0}; R) \tag{34}$$

$$\chi_H = \chi_{H0} + (\chi_0 - \chi_{H0}) \exp\left[-\left(\frac{R - R_f}{R - R_t} \xi_{\chi_H} \right)^2 \right] \tag{35}$$

$$\chi_L = \chi_{L0} + (\chi_{Lf} - \chi_{L20}) \exp\left[-\left(\frac{R - R_f}{R - R_t} \xi_{\chi_L} \right)^2 \right], \tag{36}$$

where the semiaxis ratios are $\chi_{H,L} = b_{H,L}/a_{H,L}$. $\xi_{H,L}$ is a free parameter. These laws do by no means restrict the independent variation of the shape along the partially overlapping region, since $\xi_{H,L}$ can have any value [29]. One obtains the total (contracted) mass inertia tensor $B(R)$ involving all coordinate couplings:

$$B_{b_L, \chi_H, \chi_L}(R) = B_{b_L b_L} \left(\frac{db_L}{dR} \right)^2 + 2B_{b_L \chi_H} \frac{db_L}{dR} \frac{d\chi_H}{dR}$$

$$+ 2B_{b_L \chi_L} \frac{db_L}{dR} \frac{d\chi_L}{dR} + 2B_{b_L R} \frac{db_L}{dR}$$

$$+ B_{\chi_H \chi_H} \left(\frac{d\chi_H}{dR} \right)^2 + 2B_{\chi_H \chi_L} \frac{d\chi_H}{dR} \frac{d\chi_L}{dR}$$

$$+ 2B_{\chi_H R} \frac{d\chi_H}{dR} + B_{\chi_L \chi_L} \left(\frac{d\chi_L}{dR} \right)^2$$

$$+ 2B_{\chi_L R} \frac{d\chi_L}{dR} + B_{RR}. \tag{37}$$

These calculations allow us finally to obtain the value of the nuclear mass inertia for intersected spheroids, a typical shape for fission such as binary configuration.

The action integral K_{fis}, hence the WKB penetrability P_{fis} is now ready to be calculated:

$$P_{fis} = \exp[-K_{fis}(b_l, \chi_H, \chi_L; R)], \tag{38}$$

where:

$$K_{fis}(b_l, \chi_L, \chi_H; R)$$
$$= \frac{2}{\hbar} \int_{(fis)} \left[2B_{b_L, \chi_H, \chi_L(R)}(R) E_b(R)_{b_L, \chi_H, \chi_L} \right]^{1/2} dR. \tag{39}$$

Finally, the half-life can be calculated with the well-known formula:

$$lg(T_{sf}) = -20.54 + lg[1$$
$$+ \exp(2K_{fis}(b_l, \chi_L, \chi_H; R)] - lg(2E_{zp}). \tag{40}$$

E_{zp} is the zero point vibration energy in the fission evolved direction (symmetry axis).

The dynamical trajectory of the fission path is taken as the least action integral value. The numerical minimization takes place within the multidimensional space of deformation $(b_L, \chi_H, \chi_L; R)$, with the distance between centers as the principal coordinate. The action integral is calculated along every segment of the multidimensional grid. The sequence of this mesh points, which provides the minimal K_{fis} value, is the final fission trajectory. One has to keep in mind that here the procedure is fulfilled for every fission channel considered from the beginning with $(A_H, Z_H; A_L, Z_L)$ fixed.

IV. RESULTS AND DISCUSSION

The superheavy nucleus ^{298}Fl has been chosen as it is considered a possible double-magic ($Z = 114, N = 184$) system with a greater chance for stability. Two fission valleys have been taken under scrutiny, Sn and Pb, due to their proton shell closures. One verifies the veracity of the idea that negative shell corrections will induce a barrier lowering during the overlapping region. The influence of the intermediary configuration upon the intersected level schemes, as well as on the mass inertia should determine the final fission barrier and consequently the half-life of every reaction channel.

A. Pb fission valley

The strong double shell closures ($Z_{Pb} = 82, N_{Pb} = 126$) fragment is chosen as the center of the heavy fragment mass range of the reaction partners. The first energy term, the macroscopic Yukawa-plus-exponential one, has been calculated for a wide range of Pb neutron number ($100 \leqslant N_{Pb} \leqslant 158$). Some of the macroscopic evolution curves are displayed in Fig. 1, as a function of the reduced distance between centers. The general trend is evident: as the Pb neutron
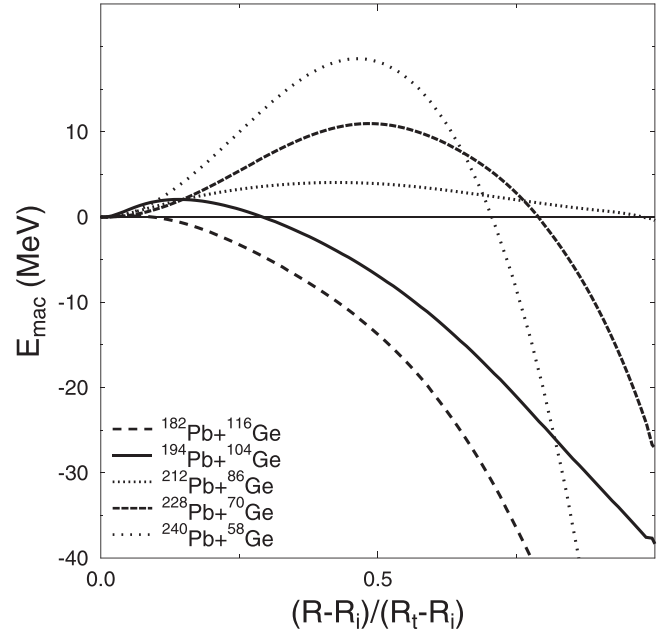

FIG. 1. Macroscopic barriers for Pb-accompanied fission channels from ^{298}Fl as a function of the reduced distance between centers.

number increases, so does the height and the width of the charged liquid drop barrier. The ^{182}Pb reaction has practically no macroscopic barrier (0.233 MeV height) and a very narrow width. As one goes towards greater mass asymmetry, the macroscopic barriers increases considerably.

The reactions have been taken with an increase of four-mass units step for Pb and Ge starting with ^{182}Pb. The trend in increasing the inertia tensor and decreasing the subsequent logarithm of the penetrability is the same for the reactions, which have been skipped, but the figures are clearer with a larger mass number step. The fact that one takes a six-mass units from ^{90}Ge to ^{96}Ge is due to the necessity of plotting the double-magic ^{208}Pb reaction.

The shell corrections for Pb reactions make all the difference for the fissioning system, as one can see in Fig. 2. No matter what reaction channel is chosen, a first negative minimum is always present, opening the possibility of a quasistable ground state. An almost -10 MeV shell corrections value is reached for the parent nucleus ^{298}Fl in all cases. The first part of reactions, neutron-poor Pb one (left-hand plot) display a second minimum, clearly generating a double-humped final barrier. The neutron-richer reactions (right-hand plot) have higher values for the total shell corrections. Also the second minimum disappeared or takes place beyond the scission point. So far, for the neutron-richer Pb partner the binary shell corrections are not favorable to fission.

The final values for the heights of macroscopic Y + E type (E_{mac}) and total fission barriers (E_b) are drawn in Fig. 3. The neutron-poor Pb reactions have close to zero Y + E barriers, but go up to about 8.4 MeV height when the shell corrections are added. The fission barrier height increases drastically as the Pb neutron number N_{Pb} is larger. Even the $N_{Pb} = 126$ has no major influence on the trend. This is due to the fact that overlapping level schemes do not bear the
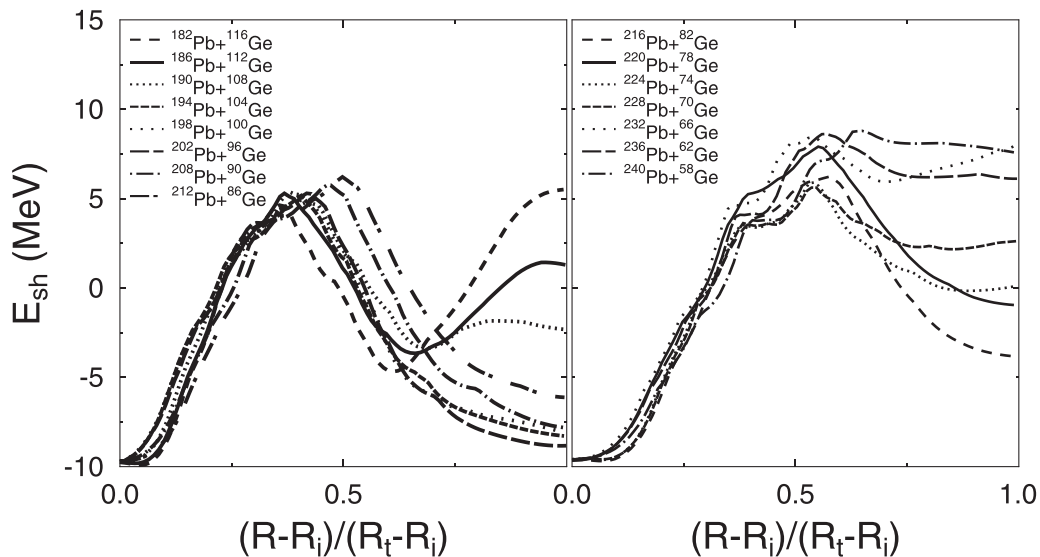
FIG. 2. Shell corrections for Pb-fragment isotopes fission channels from from ^{298}Fl, double-humped (left-hand plot) and single-humped (right-hand plot) evolution, against the reduced distance between centers.

peculiarities of the separated ones. Moreover, it is clear from this statical behavior that the fissioning system displays the largest reduction of the barrier with the tendency towards more symmetrical mass division.

The dynamics is completed with the mass tensor calculation. The inertial parameters are decisive for the possible change of the barrier and for any effect on the fission probability. The influence of the mass tensor is such that the system can be driven towards a higher deformation energy values, should that lower the total action integral. The evolution of
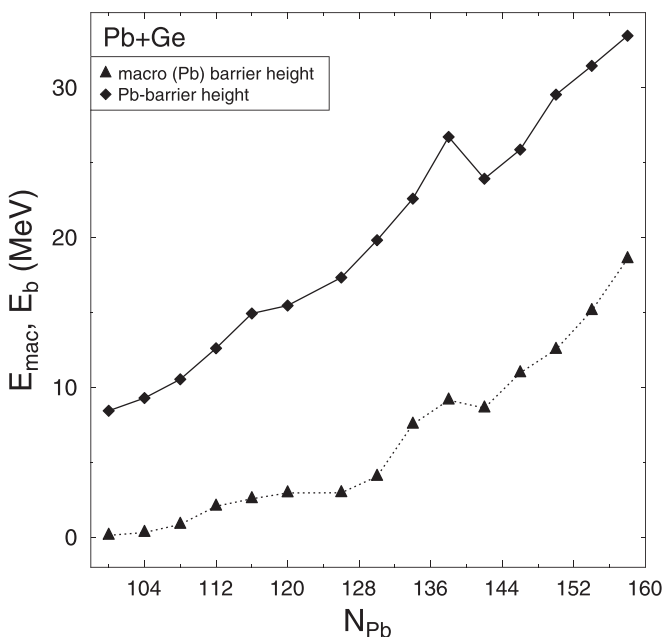
FIG. 3. Macroscopic (full triangle) and final (full diamond) fission barrier heights as function of the Pb neutron number N_{Pb}, for Pb-fission channels from ^{298}Fl. The difference emphasize the shell correction influence.

all the components of the mass tensor, together with the total value B in units of nucleon mass m_0, is presented in Fig. 4 for the most symmetric Pb-channel reaction (^{182}Pb + ^{116}Ge). All the ten possible couplings between the free coordinates vary from the parent value up to the final touching configuration one. The final value for the total, contracted inertia B is of course equal to reduced mass of the ^{182}Pb + ^{116}Ge reaction. This picture gives a first understanding of the difference against the constant reduced mass type of calculation in the WKB method. A comparison between all the mass tensor values for the Pb-valley reactions is presented in Fig. 5, as functions of the reduced distance between centers. There is a clear sudden increase at the beginning of the process, especially for more mass symmetric reactions. This behavior is known as being the most abrupt change of inertia when disrupting the parent shape. A maximum in the overall increasing behavior is always present. The exception is interesting: the only monotonous evolution takes place for ^{216}Pb + ^{82}Ge, where besides the $Z_{Pb} = 82$ proton closure, there is the Ge-neutron closure, $N_{Ge} = 50$, so the reaction is double magic. The final value, at the touching point, is obviously equal to the reduced mass of each reaction.

With the deformation energy and the mass tensor evolution along the splitting process, one calculates the action integral $K_{(fis)}$ over the whole space of deformation. As the result of minimization through the grid of coordinates, the WKB penetrability $P_{(fis)}$ is obtained. The logarithms of the penetrabilities with the binary Werner-Wheeler inertia, lgP_{WW}, together with the ones calculated with the reduced mass lgP_μ, are presented in Fig. 6, for all possible Pb-accompanied fission reactions from ^{298}Fl. All Werner-Wheeler-type penetrabilities are higher than the ones where one considers only the reduced mass. This trend is clear along the whole splitting process, from parent, through overlapping and finally separated fragments: penetrabilities are larger when mass tensor components are introduced against the reduced mass.
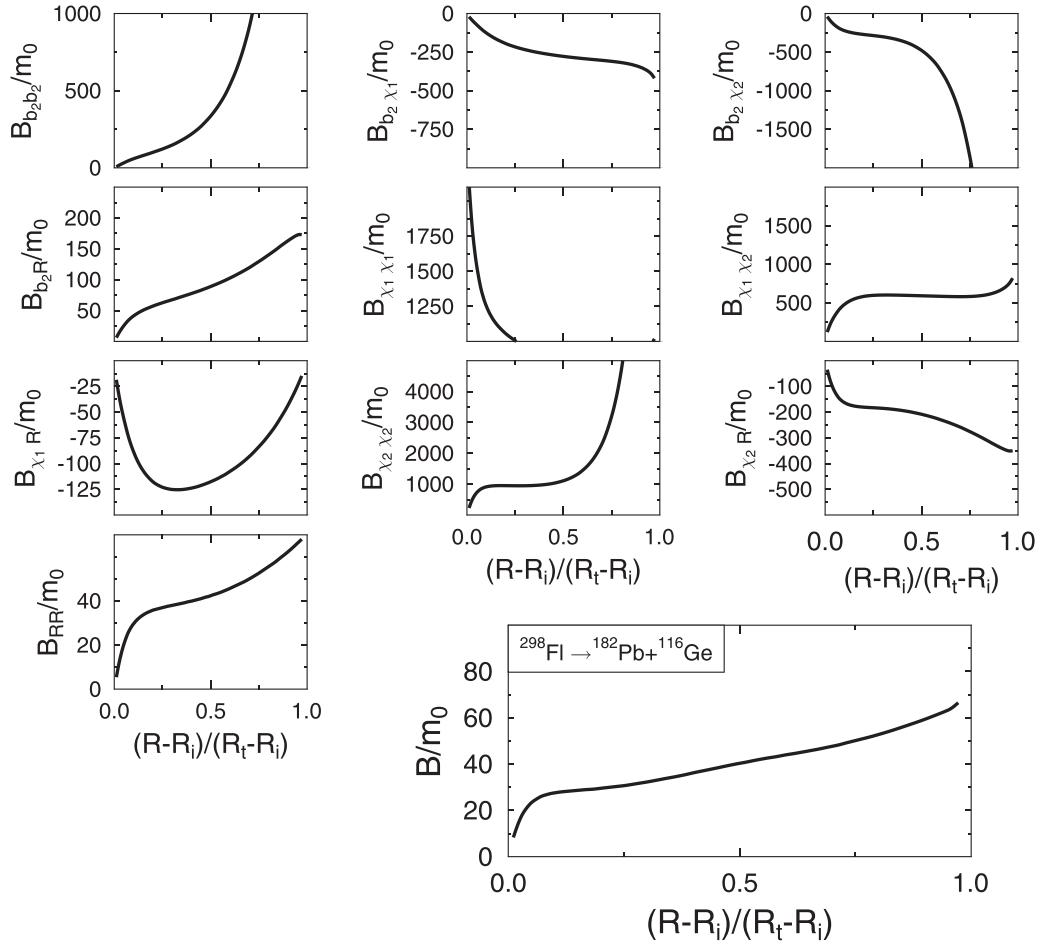
FIG. 4. Inertia tensor coupling components B_{ij} and total mass inertia B after contraction along the distance between centers R, for ^{298}Fl $\rightarrow$ ^{182}Pb $+$ ^{116}Ge reaction.
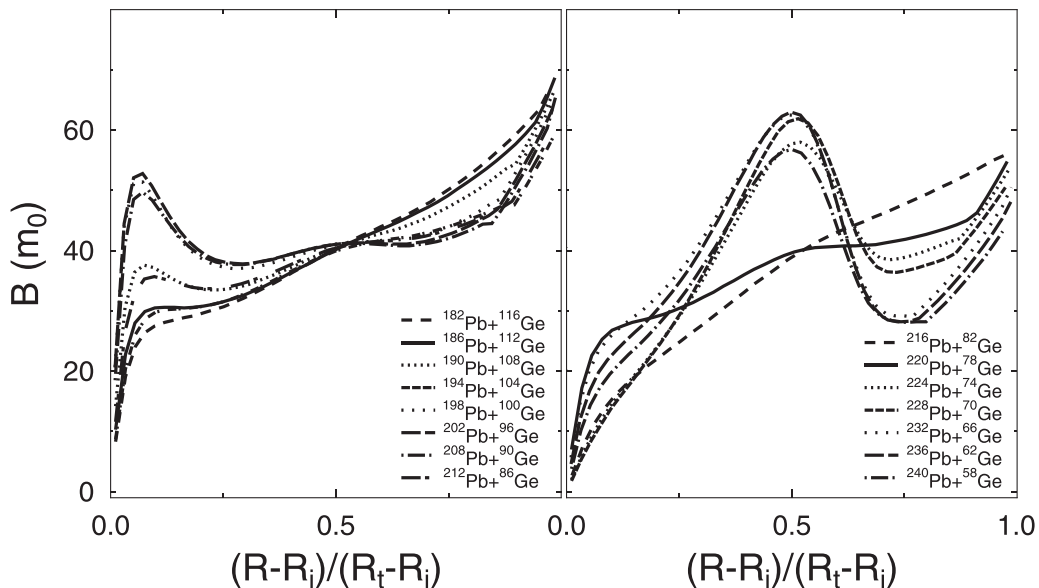

FIG. 5. Comparison between the evolution of the mass inertia tensors for the Pb-accompanied fission channels from ^{298}Fl with the reduced distance between centers. One remarks the smooth behavior for the proton double-magic reaction ^{216}Pb $+$ ^{82}Ge.
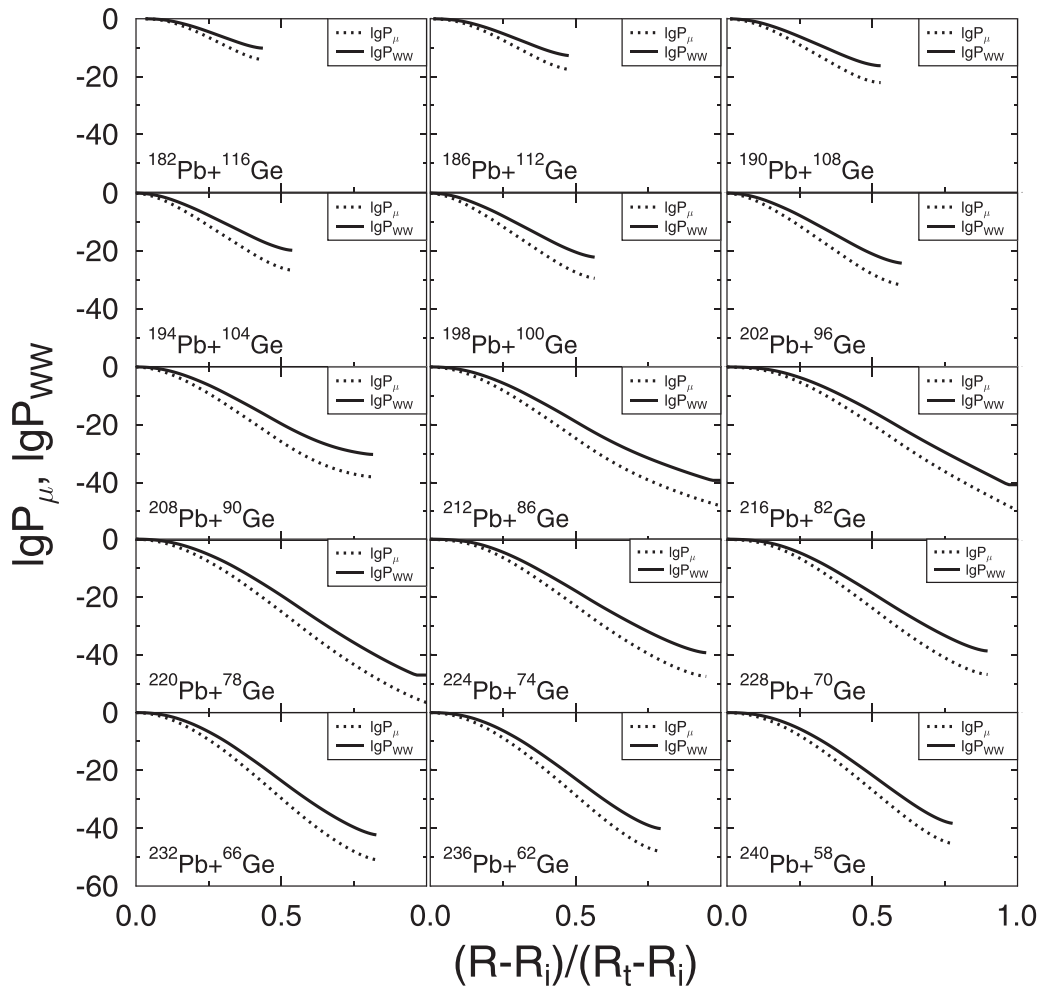
FIG. 6. Comparison between penetrability logarithm evolution calculated with the Werner-Wheeler mass tensor inertia (full line) and with the reduced mass (dotted line), for the Pb-fission channels from ^{298}Fl, as a function of the reduced elongation. The highest value is obtained for the most symmetric channel ^{192}Pb.
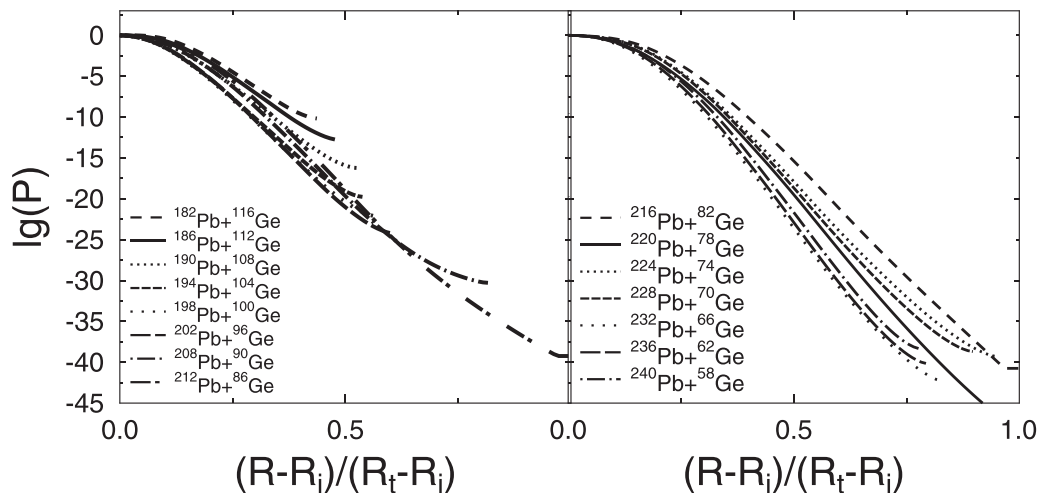

FIG. 7. Evolution of the WKB penetrabilities for all Pb-accompanied fission channels from the superheavy ^{298}Fl. The shortest path involves also the highest penetrability value (^{182}Pb + ^{116}Ge), and the fastest exit point.
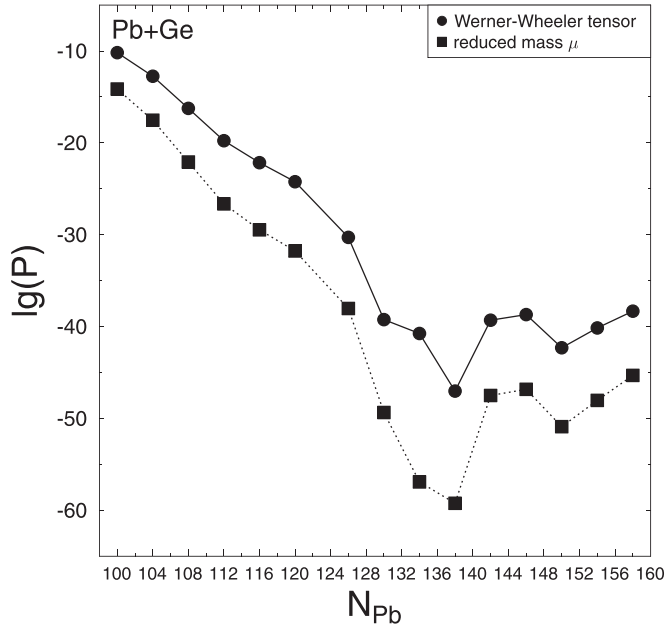
FIG. 8. Comparison between Werner-Wheeler (full circle) and reduced mass (full square) penetrability logarithms, against the Pb-fragment neutron number N_{Pb}. The highest value corresponds to ^{182}Pb-fragment reaction.

FIG. 10. Comparison between the macroscopic (full triangle) and total deformation (full diamonds) fission barrier heights for Sn-fragment fission channels, as functions of the Sn neutron number N_{Sn}. The differences reveal the shell correction influence.

A comparison between the penetrabilities for all the fission channels with Pb as the heavy partner from ^{298}Fl is shown in Fig. 7. The left-hand plot contains the more mass-symmetrical reactions. The ^{182}Pb-channel final penetrability value is the largest. Moreover, the fission path is the shortest for this
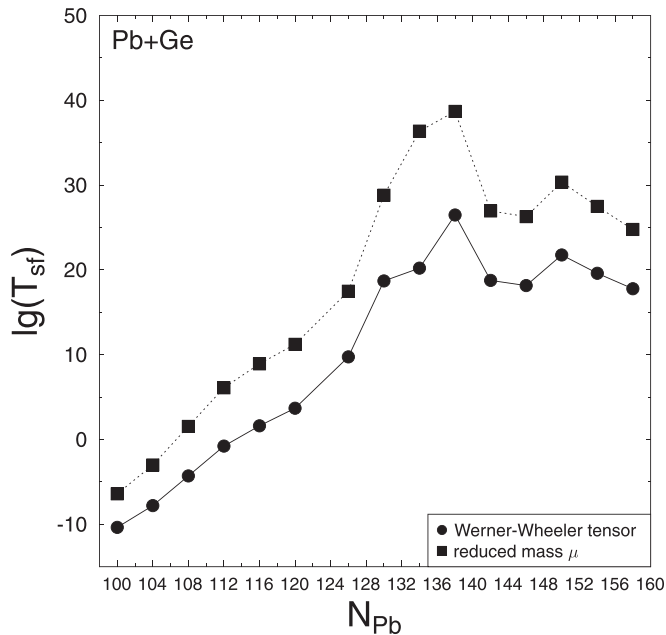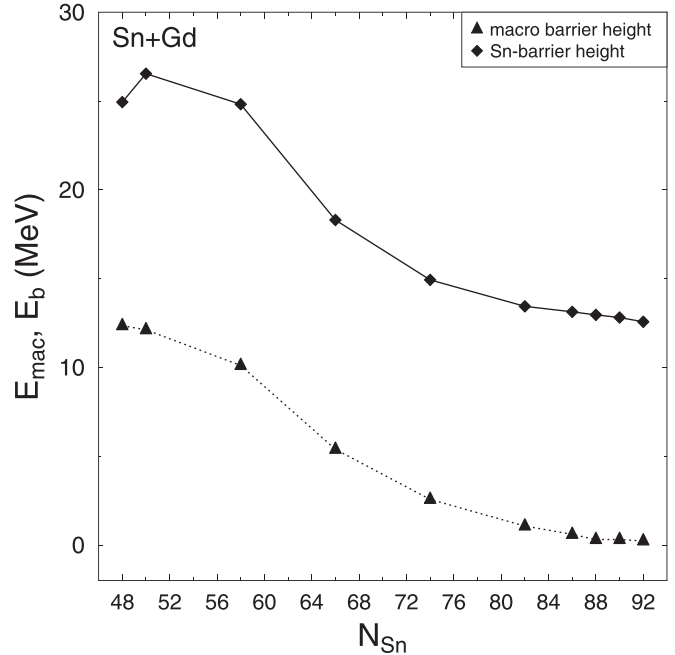

FIG. 9. Comparison between Werner-Wheeler (full circle) and reduced mass (full square) half-life logarithms for Pb-reactions fission channels. The lowest values corresponds to the most mass-symmetric reactions.

reaction. One can see that the final point ends way before the total splitting takes place. The situation is the same for the majority of these channels. This is a well-known effect for superheavy elements, observed even in one-center-type calculations, within a large $\{\beta_\lambda\}$ deformation space. As the mass asymmetry increases, the penetrability decreases. At the same time (left-hand plot) the system is still under the barrier when it gets closer to the scission point, so the width of the barrier also increases for an increase of reaction mass asymmetry.

The differences between the final values of penetrabilities calculated with the Werner-Wheeler mass tensor and with the reduced mass, are more clearly seen in Fig. 8, plotted against the Pb neutron number N_{Pb}. The highest value corresponds to the most mass-symmetrical reaction, ^{182}Pb + ^{116}Ge. The penetrability decrease is abrupt, almost proportional with the increase in mass asymmetry. A very low value ($lgP \approx -59.1$) corresponds to ^{220}Pb-fission channel. This reaction has also the largest barrier width. One has to mention that the ^{208}Pb double-magic reaction produces no maximum in penetrability, hence there is no advantage from the final negative shell corrections of the proton and neutron shell closures. The following reactions have higher penetrabilities, still large values compared to the more symmetric ones. These differences come from the macroscopic energy, but also from the differences in shell corrections. The penetrabilities calculated only with the reduced mass are obviously underestimated.

The penetrability influence on the half-life values is plotted in Fig. 9, where their logarithms of Werner-Wheeler type lgT_{sf} are displayed (full circles) together with the values calculated with the reduced mass (full squares). All the Pb-fission channels have a shorter lifetime when calculated with the mass

TABLE I. Fission barrier heights, logarithms of penetrabilities, and half-lives for the Pb-fragment fission channels from ^{298}Fl.

Reaction	$E_b(MeV)$	lgP_μ	lgP_{WW}	lgT_μ	lgT_{WW}
^{182}Pb + ^{116}Ge	8.443	−14.136	−10.177	−6.404	−10.363
^{186}Pb + ^{112}Ge	9.290	−17.553	−12.745	−3.007	−7.795
^{190}Pb + ^{108}Ge	10.544	−22.083	−16.243	1.543	−4.297
^{194}Pb + ^{104}Ge	12.606	−26.640	−19.764	6.1	−0.776
^{198}Pb + ^{100}Ge	14.122	−29.463	−22.154	8.923	1.614
^{202}Pb + ^{96}Ge	15.461	−31.764	−24.228	11.224	3.688
^{208}Pb + ^{90}Ge	17.333	−38.027	−30.286	17.487	9.743
^{212}Pb + ^{86}Ge	19.816	−49.350	−39.239	28.810	18.699
^{216}Pb + ^{82}Ge	22.591	−56.906	−40.749	36.366	20.209
^{220}Pb + ^{78}Ge	26.706	−59.233	−47.018	38.693	26.478
^{224}Pb + ^{74}Ge	23.915	−47.497	−39.302	26.957	18.762
^{228}Pb + ^{70}Ge	25.863	−46.825	−38.693	26.285	18.153
^{232}Pb + ^{66}Ge	29.533	−50.892	−42.302	30.352	21.762
^{236}Pb + ^{62}Ge	31.454	−48.031	−40.145	27.491	19.605
^{240}Pb + ^{58}Ge	33.462	−45.311	−38.320	24.771	17.780

Table I presents the fission barrier heights E_b, logarithms of penetrability for mass tensor lgP_{WW} and reduced mass lgP_μ, and the logarithms for the corresponding half-lives lgT_{WW} and lgT_μ for all Pb channels. As expected, the lowest barrier (with also the narrowest width), produces the highest penetrability, hence the shortest half-life ($lgT_{WW} = -10.363$). The corresponding value calculated with the reduced mass is also the lowest. Also, short values are evident for $^{186-198}$Pb, as belonging to the quasisymmetrical mass domain of fragmentation. One would affirm that $^{182-190}$Pb channels have the best chances to be detected in this fragment mass region. The less probable Pb-channel reaction is ^{220}Pb, with the largest lifetime and lowest penetrability value. After that, a decrease in half-life value is observed for the last three channels, but the values are also high, having a low fission probability. The main conclusion to be drawn is that the system prefers symmetric mass fragmentation, not being influenced by shell closures of the final fragments.

tensor. The most probable channel to be detected is the most mass symmetrical one, ^{182}Pb + ^{116}Ge. There is no evident influence coming from the double-magic ^{208}Pb partner as being advantaged by double magicity.

B. Sn fission valley

The same procedure is applied for the channels containing Sn isotopes. Their range has been somehow centered around the double-magic ^{132}Sn (range $^{198-142}$Sn). One has to mention
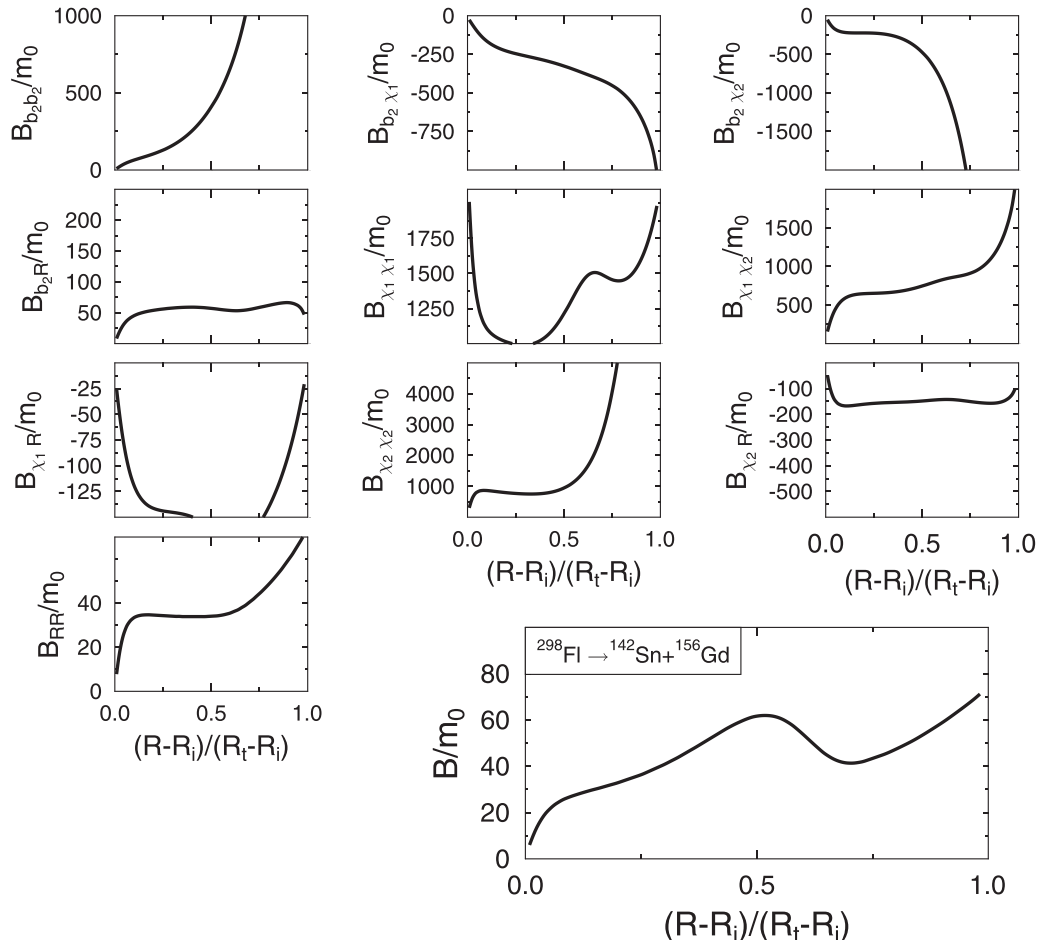

FIG. 11. Tensor components for all coupling coordinates within the Werner-Wheeler calculation, B_{ij} and the total contracted mass inertia value B for the most symmetric Sn-accompanied reaction ^{142}Sn + ^{156}Gd.
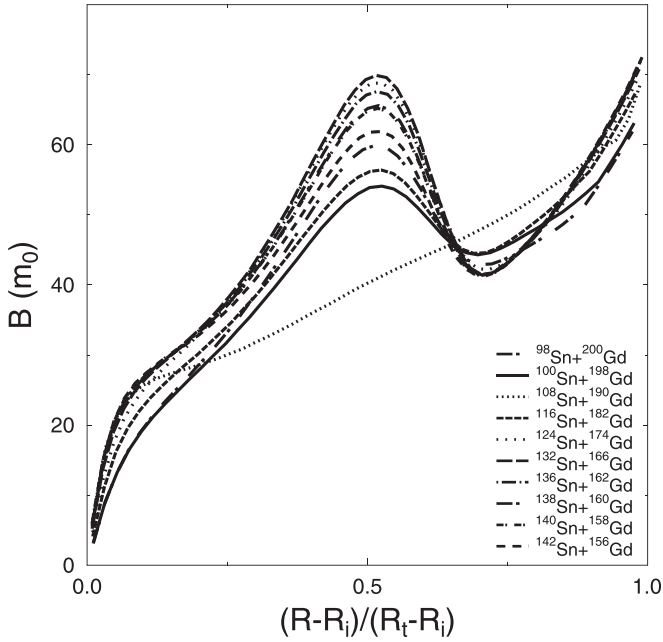
FIG. 12. The mass inertia tensor evolution against the reduced distance between centers for all Sn-fragment isotopes reactions from ^{298}Fl. The maximum corresponds to closing the exit point of the barrier. The irregular smooth increase belong to the double-magic reaction ^{108}Sn + ^{190}Gd.

FIG. 14. The penetrability evolution along the reduced distance between centers for the Sn-accompanied fission channels from ^{298}Fl. The highest value corresponds to the mass symmetric reaction ^{142}Sn + ^{156}Gd. The same reaction has the shortest exit point from the barrier.

that the binary configurations within this group tend towards mass symmetry as the Sn neutron number increases, so the opposite from the Pb cases. The consequence from this trend upon the fission barriers can be observed in Fig. 10, where the heights of the Sn-reaction deformation energies have been plotted. The Sn-channel barriers have a reversed behavior with respect to the increase of the Sn neutron number N_{Sn}. Poor neutron Sn channels have both a higher macroscopic Y + E type (full triangle) and total fission barrier height (full diamonds). As N_{Sn} increases, the system becomes more sym-

metric in mass fragmentation, though the charge asymmetry is the same. One can see that two double-magic fragments, ^{100}Sn and ^{132}Sn, have no influence in the almost monotonous decrease of the barrier heights. The heights follow more or less the macroscopic behavior. Evidently, the differences are due to the shell effects.

To complete the dynamics, the Werner-Wheeler mass tensor has been computed for this group of reactions. The behavior for all the coordinate coupling components B_{ij} ($i, j = b_L, \chi_H, \chi_L, R$) and the total value B of the tensor after contraction along R coordinate, is plotted in Fig. 11, for the most mass symmetric reaction ^{142}Sn + ^{156}Gd. The last value B takes, at the touching point configuration, the reduced mass one, the rest are beneath it. This evolution suggest a more favorable penetrability than the one using only the reduced mass μ. A comparison between the mass inertia evolutions with the reduced distance between centers for all Sn channels is drawn in Fig. 12. The increasing behavior up to 0.5 of the reduced distance is common status. After a second minimum at $R_n \approx 0.75$, the inertia increases again. One has to mention that the second minimum corresponds more or less to the scission point of the barriers. A somewhat different trend can be observed for ^{108}Sn + ^{190}Gd, with an absolute monotonous increase. Again, this reaction is a double-magic one, with a neutron closure at $N = 126$ for Gd fragment, similarly with the Pb case.

The difference between the reduced mass (lgP_μ) and the Werner-Wheeler inertia tensor (lgP_{WW}) calculations of the WKB penetrabilities is plotted in Fig. 13 for the Sn channels, as functions of the reduced distance between centers. One can see the highest values corresponding to the more mass
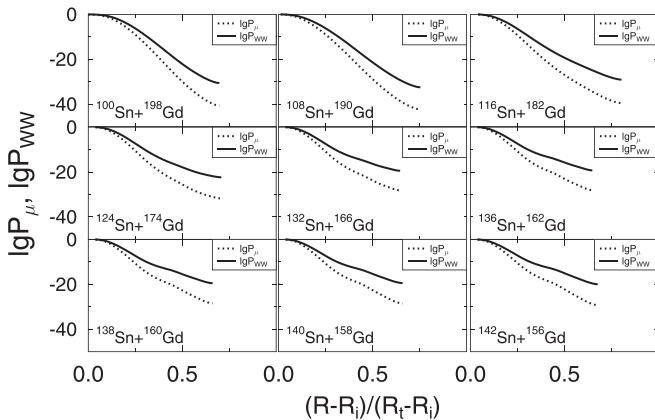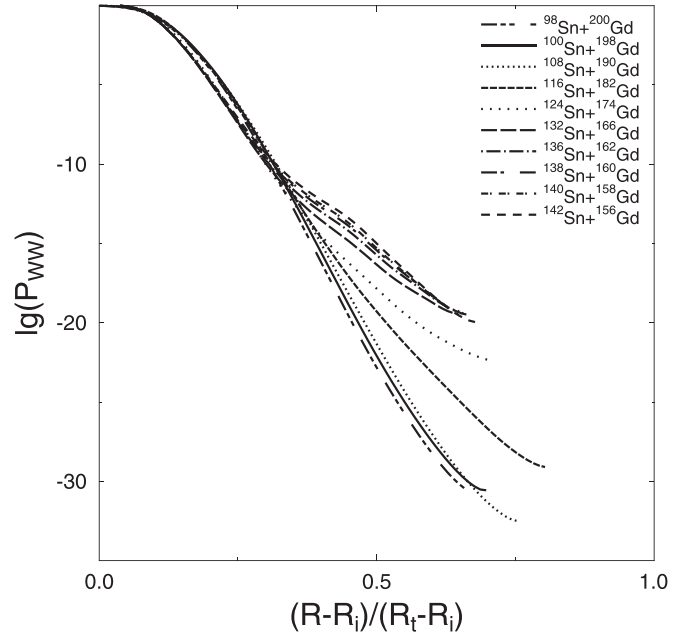

FIG. 13. Comparison between WKB penetrabilities calculated with the reduced mass (dotted line) and Werner-Wheeler mass tensor (full line). The largest values are obtained for the most mass symmetrical reaction channels ^{142}Sn + ^{156}Gd. All penetrability values are higher for the Werner-Wheeler-type calculation.
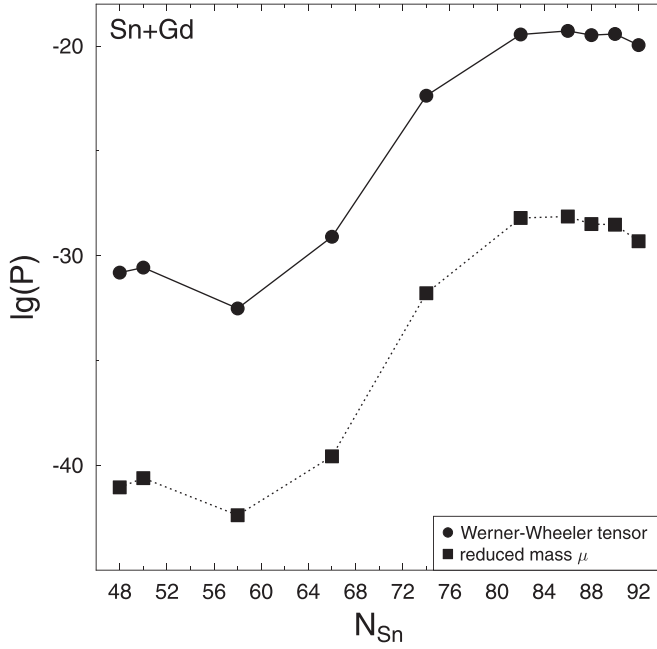
FIG. 15. Penetrability logarithms for reduced mass (full square) and Werner-Wheeler calculation (full circle) for the Sn-fission channels against the Sn neutron number N_{Sn}. One has higher values when the mass inertia tensor is taken into account. The highest penetrability value yields for the neutron-richest Sn isotope.
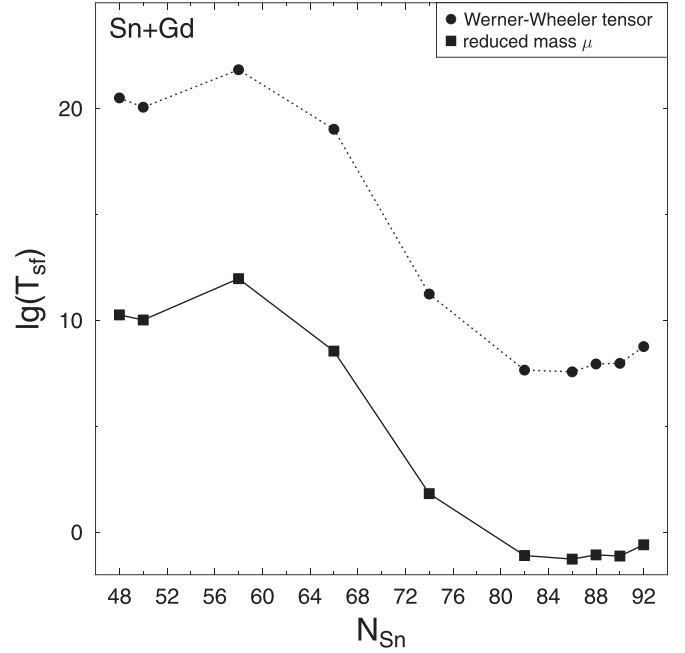

FIG. 16. Logarithms of the spontaneous fission half-lives for reduced mass (full squares) and Werner-Wheeler (full circles) calculations, for Sn-isotope channels against the Sn neutron number N_{Sn}. The group with the shortest half-life lies around $N_{Sn} \approx 82$–92.

symmetric reactions. As the system advances through tunneling, elongation increases and penetrability decreases. In all cases, the mass inertia penetrability is higher than the one calculated with the reduced mass. The penetrability evolution for the Sn group is plotted for comparison as a function of elongation in Fig. 14. The lowest values correspond to the most asymmetric reactions ($^{98-108}$Sn), and the highest ones are obtained for the quasisymmetric ones ($^{140-142}$Sn). Not only these latter reactions are favored, but also their exit points from the barrier are shorter. The scission ($R = R_t$) is not reached and the tunneling process ends at $(R - R_i)/(R_t - R_i) \approx 0.7$. One can state that a certain fission channel is decided before the total fragment separation. The values of the penetrabilities lgP for the Sn-fission channels are plotted in Fig. 15, for reduced mass (full square) and Werner-Wheeler (full circle) mass inertia. There is no influence from the double magicity of ^{100,132}Sn. The values increase only as the Sn neutron number (N_{Sn}) increases. The amount of the increase is highly influenced by the shell corrections, especially for the cases when the macroscopic barrier is almost zero. One can see that penetrabilities are always higher for Werner-Wheeler inertia-type calculations.

The corresponding logarithms of half-lives are drawn in Fig. 16. There are orders of magnitude difference between the two types of calculations. The rigid reduced mass cannot properly describe the dynamic evolution of the deformation coordinate couplings. The influence of these couplings is reflected in this plot by the much lower values of the lifetimes. One emphasize that these characteristics apply to certain,

established fission channels. The lowest half-life values correspond to $^{132-142}$Sn channels.

The values of the barrier heights, logarithm of penetrability and of the corresponding half-life are presented in Table II for Werner-Wheeler inertia and reduced mass calculation, for the Sn-fragment isotope group. The highest penetrability, hence the shortest lifetime is seen for ^{136}Sn, belonging to the last four most mass quasisymmetrical reactions ($^{136-142}$Sn). The lifetimes differences are very small for this group, but very large compared to $^{98-124}$Sn one. One can affirm that for the quasisymmetrical group the differences are influenced mainly by the shell corrections, as can be seen in Fig. 10 and reflected in Table II.

TABLE II. Y+E maximum $E_{mac}^{(max)}$, fission barrier height E_b and their position on the reduced distance R_n between centers for Sn-channel reactions.

Reaction	$E_b(MeV)$	lgP_μ	lgP_{WW}	lgT_μ	lgT_{WW}
^{98}Sn + ^{200}Gd	24.94	−41.05	−30.81	20.51	10.27
^{100}Sn + ^{198}Gd	26.54	−40.61	−30.57	20.07	10.03
^{108}Sn + ^{190}Gd	24.82	−42.38	−32.52	21.84	11.98
^{116}Sn + ^{182}Gd	18.30	−39.57	−29.10	19.03	8.56
^{124}Sn + ^{174}Gd	14.93	−31.79	−22.37	11.25	1.83
^{132}Sn + ^{166}Gd	13.44	−28.20	−19.45	7.66	−1.09
^{136}Sn + ^{162}Gd	13.13	−28.13	−19.28	7.58	−1.26
^{138}Sn + ^{160}Gd	12.96	−28.49	−19.48	7.95	−1.06
^{140}Sn + ^{158}Gd	12.81	−28.52	−19.42	7.98	−1.12
^{142}Sn + ^{156}Gd	12.57	−29.31	−19.95	8.77	−0.59

V. CONCLUSIONS

A binary macroscopic-microscopic based on the two-center shell model plus dynamics method has been established in order to study particular fission channels. The method has been applied to two groups of fission valleys, for Pb and Sn isotopes as main fragments. Since the macroscopic barrier part is very low, the shell corrections dominate the barrier behavior. The dynamics has been completed with the binary Werner-Wheeler inertia tensor. For Pb isotopes, the poor neutron Pb partners are favored, with the shortest lifetime for ^{182}Pb of value lgT_{182}Pb $= -6.404$, followed by ^{186}Pb with -3.007. As the neutron number increases, the penetrabilities are smaller and fission probability decreases. At the same time, the system becomes more mass asymmetric.

The second fission valley has been chosen for Sn-isotopes partners, due to their possible double magicity around $N_{Sn} = 50$, 82. It turns out that these neutron closures have no influence upon lowering the barrier, but it influences the shape of the total deformation energy, hence the penetrability. The overlapping region does not feel any influence from the separated fragment magicity. Contrary to the Pb group, the penetrability increases with increasing the Sn neutron number within the Sn valley, generating a lifetime of minimum lgT_{136}Sn $= -1.26$, followed closely by its neighbor ^{140}Sn with -1.12. This trend correspond to the tendency towards a more symmetrical mass fragmentation, similar to the Pb group. The decay reactions ^{182}Pb $+ ^{116}$Ge, ^{186}Pb $+ ^{112}$Ge, and ^{136}Sn $+ ^{162}$Gd and ^{140}Sn $+ ^{158}$Gd are favored fission channels from the superheavy compound nucleus ^{298}Fl.

ACKNOWLEDGMENTS

[1] J. R. Nix, Calculation of fission barriers for heavy and superheavy nuclei, Annu. Rev. Nucl. Sci. **22**, 65 (1972)

[2] A. Baran, K. Pomorski, A. Lukasiak, and A. Sobiczewski, A dynamic analysis of spontaneous fission half-lives, Nucl. Phys. A **361**, 83 (1981)

[3] I. Muntian and A. Sobiczewski, Fission Barriers of Heavy and Superheavy Nuclei, in *Structure and Dynamics of Elementary Matter*, edited by W. Greiner and M. G. Itkis, NATO Science Series, Vol. 166 (Springer, Dordrecht, 2004).

[4] M. Kowal, P. Jachimowicz, and A. Sobiczewski, Fission barriers for even-even superheavy nuclei, Phys. Rev. C **82**, 014303 (2010).

[5] K. Mazurek, P. N. Nadtochy, E. G. Ryabov, and G. D. Adeev, Fission fragment distribution within dynamical approach, Eur. Phys. J. A **53**, 79 (2017).

[6] L. L. Liu, X. Z. Wu, Y. J. Chen, C. W. Shen, Z. X. Li, and Z.G. Ge, Study of fission dynamics with three-dimensional Langevin approach, Phys. Rev. C **99**, 044614 (2019).

[7] K. Pomorski, A. Dobrowolski, B. Nerlo-Pomorska *et al.*, On the stability of superheavy nuclei Eur. Phys. J. A **58**, 77 (2022).

[8] J. A. Maruhn, J. Hahn, H.-J. Lustig, K.-H. Ziegenhain, and W. Greiner, Quantum fluctuations within the fragmentation theory, Prog. Part. Nucl. Phys. **4**, 257 (1980).

[9] R. K. Gupta, M. Sharma, S. Singh, R. Nouicer, and C. Beck, Fission and cluster decay of the ^{76}Sr nucleus in the groundstate and formed in heavy-ion reactions, Phys. Rev. C **56**, 3242 (1997).

[10] A. S. Jensen and J. Damgaard, Shell effects in a paired nucleus for finite excitation energies, Nucl. Phys. A **203**, 578 (1973).

[11] S. Kumar, M. Balasubramaniam, R. K. Gupta, G. Muenzenberg, and W. Scheid, The formation and decay of superheavy nuclei produced in ^{48}Ca-induced reactions, J. Phys. G: Nucl. Part. Phys. **29**, 625 (2003).

[12] G. Royer, Alpha emission and spontaneous fission through quasi-molecular shapes, J. Phys. G: Nucl. Part. Phys. **26**, 1149 (2000).

[13] G. Royer, N. Mokus, and J. Jahan, Geometric shapes and relationships of some one-body and multibody leptodermous distributions, Phys. Rev. C **95**, 054610 (2017).

[14] K. P. Santhosh, C. Nithya, and T. A. Jose, Decay modes of superheavy nuclei using a modified generalized liquid drop model and a mass-inertia dependent approach for spontaneous fission, Phys. Rev. C **104**, 024617 (2021).

[15] P. Moeller, A. J. Sierk, T. Ichigawa, and H. Sagawa, Nuclear ground-state masses and deformations, At. Data Nucl. Data Tables **109-110**, 1 (2016).

[16] J. M. Allmond and J. L. Wood, Empirical moments of inertia of axially asymmetric nuclei, Phys. Lett. B **767**, 226 (2017).

[17] K. P. Santhosh and C. Nithya, Theoretical predictions on the decay properties of superheavy nuclei Z=123 in the region 297 $\leqslant$ A $\leqslant$ 307, Eur. Phys. J. A **52**, 371 (2016).

[18] P. R. Chowdhury, C. Samanta, and D. N. Basu, Alpha-decay half-lives of new superheavy elements, Phys. Rev. C **73**, 014612 (2006).

[19] C. Samanta, P. R. Chowdhury, and D. N. Basu, Predictions of alpha decay halflives of heavy and superheavy elements, Nucl. Phys. A **789**, 142 (2007).

[20] P. N. Nadtochy, E. G. Ryabov, A. V. Karpov, and G. D. Adeev, Transport coefficients for modeling fission dynamics, Comput. Phys. Commun. **275**, 108308 (2022).

[21] Y. Qiang, J. C. Pei, and P. D. Stevenson, Fission dynamics of compound nuclei: Pairing versus fluctuations, Phys. Rev. C **103**, L031304 (2021).

[22] D. T. Akrawy, A. I. Budaca, G. Saxena, and A. H. Ahmed, Generalization of the screened universal alpha-decay law by asymmetry and angular momentum, Eur. Phys. J. A **58**, 145 (2022).

[23] R. A. Gherghescu and W. Greiner, Charge density influence on cold fusion barriers, Phys. Rev. C **68**, 044314 (2003).

[24] D. N. Poenaru, M. Ivascu, and D. Mazilu, Folded Yukawa-plus-exponential model for nuclei with different charge densities, Comput. Phys. Commun. **19**, 205 (1980).

[25] H. J. Krappe, J. R. Nix, and A. J. Sierk, Unified nuclear potential for heavy ion elastic scattering, fusion, fission and ground state masses and deformations, Phys. Rev. C **20**, 992 (1979).

[26] R. A. Gherghescu, Deformed two-center shell model, Phys. Rev. C **67**, 014309 (2003).

[27] H. Kroger and W. Scheid, Classical dynamical description of heavy-ion sequential fission, J. Phys. G: Nucl. Phys. **6**, L85 (1980).

[28] K. T. R. Davies, A. J. Sierk, and J. R. Nix, Effect of viscosity on the dynamics of fission, Phys. Rev. C **13**, 2385 (1976).

[29] R. A. Gherghescu and D. N. Poenaru, Two-dimensional nuclear inertia: Analytical relationships, Phys. Rev. C **52**, 2636 (1995).